Original article

Institution of MECHANICAL ENGINEERS
Journal of PROCESS MECHANICAL ENGINEERING

Proc IMechE Part E:
J Process Mechanical Engineering
0(0) 1–9

DOI: 10.1177/0954408916662088
uk.sagepub.com/jpme
SAGE

Molecular dynamics simulation study on ablation of silicon by water-jet-guided laser

Weiguo Zhou[1], Keyu Gong[1], Jie Wan[2], Lulu Quan[1], Yuchuan Chu[1] and Yong Cao[1]

Abstract

Stillinger–Weber potential and *Z*-layer energy model were adopted in molecular dynamics simulation to study the ablation of silicon by water-jet-guided femtosecond laser, and comparison was made by ablating silicon with or without water-jet cooling in our simulations. Simulation results indicated that with water-jet cooling, the thermal-affected zone could be reduced in area, and the peak of density could disappear more quickly. It was therefore concluded that water-jet-guided laser could be used to considerably improve the ablation quality of silicon.

Keywords

Molecular dynamics simulation, resolidification, thermal wave, water-jet-guided laser

Date received: 16 August 2015; accepted: 2 June 2016

Introduction

With the rapid development of microelectronics, semiconductor material has been are widely used in different types of electronic components, and silicon becomes increasingly important because of its great abundance on earth and outstanding physical and chemical characteristics. So, a lot of micro-machining techniques, including Lithographie, Galvanoformung, Abformung micro-machining, micro electric discharge machining and micro electrochemical machining, have been developed in recent years for the fabrication of microelectrical mechanical systems.

Among the micro-machining techniques, Laser processing is a very effective processing tool with such advantages of less thermal effect, no contact, high efficiency, high precision and no tool wearing.[1] Especially, the reduction of heat-affected zone in the material being processed resulting from the extremely narrow pulse width ranging from several tens to several hundreds of femtoseconds, which allows high-quality micro-fabrication to be achieved in either soft or hard or even brittle material. This is the reason why femtosecond laser is now widely used for machining, structuring and/or modifying different material to achieve its excellent performance.[2]

However, it is inevitable that the thermal wave generated during the laser processing which could lead to the irregular deformation of material during laser irradiation, such as dislocations and vacancies.[3] Thus, water-jet-guided laser is used in the ablation process in order to overcome these drawbacks.[4] Total reflection occurs in the inner surface of water because of the difference in refractive index of water and air, and the laser beam is guided by high pressure water-jet to the workpiece surface. In comparison with a conventional way of ablating silicon by laser, water-jet-guided laser micro processing has the following advantages:[2,4,5]

1. The heat-affected zone can be reduced by water-jet cooling and so, thermal residual stress and micro-cracks are reduced;
2. The roughness of machined surface is reduced because the burr caused by melting can be reduced by the scouring effect;
3. The laser energy is made more uniformly distributed within the water beam.

[1]Department of Mechanical Engineering and Automation, Harbin Institute of Technology, Shenzhen Graduate School, Shenzhen, P. R. China
[2]Department of Energy Science and Engineering, Harbin Institute of Technology, Harbin, P. R. China

Corresponding author:
Yong Cao, Department of Mechanical Engineering and Automation, Harbin Institute of Technology, Shenzhen Graduate School, Shenzhen, Guangdong 518055, P. R. China.
Email: yongc@hitsz.edu.cn

These advantages can be explained in such a way that the cooling effect of water-jet greatly reduces the heat-affected zone in the material and so, the deformation of material can be considerably reduced. Water-jet-guided laser has been well developed as an effective micro-machining technique in the past decades,[2] but the mechanism of ablation of silicon by water-jet-guided laser has not been better understood yet so far.

The research on the ablation of silicon is conducted by many researchers in the past decades. For example, Herrmann et al.[6] studied the effect of picosecond and femtosecond laser pulses on ablation surfaces. Ho et al.[7] and Watanabe et al.[8] investigated the ablation of silicon by ultrashort pulsed laser at al. The effect of water-jet was investigated by experimental techniques as in Sibailly et al.[2] Compared with experimental technique, molecular dynamics (MD) simulation has the advantage that more details can be obtained about the ablation of the material, such as the ablation process, the generation and propagation of thermal shock waves. Evolution of macro-variables, such as temperature, energy and pressure, can also be obtained. Another advantage of MD simulation is that the influence of one or more parameters can be studied separately, which is highly difficult or often even impossible to obtain through experiments. Furthermore, the physical variables, which can hardly be obtained through experimental technique, can be investigated through MD simulations. MD simulation has already been used to model the laser-material interaction for various materials, including metals,[9] organic solids[10] and semiconductor.[6,11,12]

Therefore, a model established through MD simulations, as shown in Figure 1, was employed to investigate the ablation of silicon by water-jet-guided laser. Water-jet on either side of the model was used to reduce the temperature of particles along the boundaries. This investigation involved the energy input of laser, the cooling effect of water-jet and the melting and removal of silicon. We focus only on the cooling effect of the water with regards to Si rather than taking the force interaction between water and Si for the present. The simulation results in Li et al.[13] revealed the mechanism in the thermal process and provided an insight of the complex interactions among laser, water-jet and workpiece. However, the propagation of thermal wave during laser irradiation or the utilization of water-jet laser to improve the ablation of silicon quality was not discussed in that paper. In order to achieve a better understanding, much more particles would be involved to obtain a much more accurate distribution of such physical parameters as temperature and density, etc. In addition, the cooling effect of water-jet-guided laser was studied to obtain a more accurate profile of the surface of silicon.

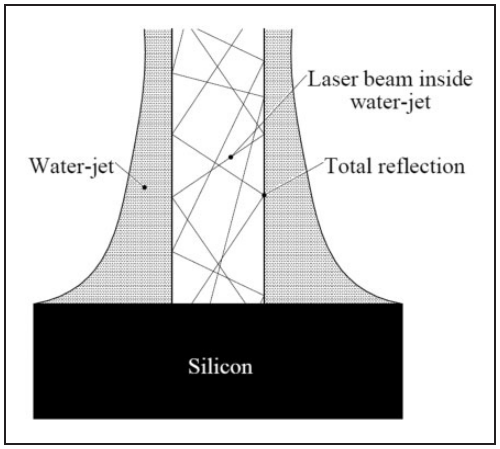

Figure 1. Schematic diagram of ablation of silicon by water-jet-guided laser.

Simulation model

MD simulations were adopted to model the ablation of silicon to gain an insight into the mechanisms of particular phenomena in this study.

Laser absorption and setup

As shown in Figure 2(a), the simulation model employed is composed of silicon and laser. The pulse lengths ($\tau_L = 100$ fs) of laser beam with uniform intensity distribution traveled in direction z and entered the system from the top $\lambda = 266$ nm were usually used for previous researches.[8] For the first 0.2 ps, the particles were damped to T_0, followed by a relaxation period of 0.8 ps which as shown in Figure 2(b), the laser was starting at $t = 1.0$ ps. The laser energy was deposited on each atom according to the Lambert–Beer's law[14]

$$I = (1 - R)I_0 e^{-\alpha z} \tag{1}$$

where R is the surface reflectivity of silicon, I_0 is the initial laser intensity and α is the linear absorption coefficient of silicon. For the present simulation, the

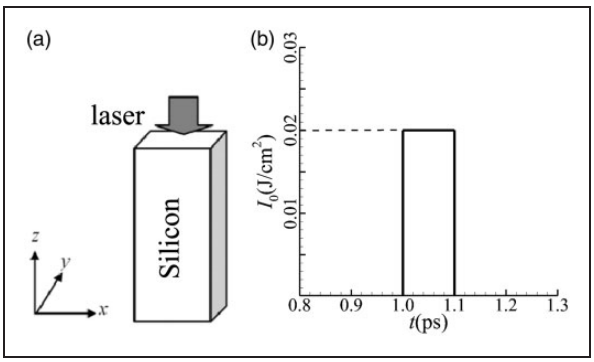

Figure 2. (a) Sketch of simulation model and (b) distribution of femtosecond laser for present simulations.

Table 1. Parameters of case II.

Quantity	Symbol	Value
Wavelength	λ	266 nm
Laser focus	D	4.34 nm
Pulse width	τ_L	100 fs
Laser fluence	I_0	0.02 J/cm^2
Number of particles	N	16,384
Surface reflectivity	R	0.474
Melting temperature	T	1683 K
Absorption coefficient	α	2.09×10^8 m^{-1}
Silicon volume	V_b	8.69 nm $\times$ 4.34nm $\times$ 8.69 nm
Computational domain	V_c	8.69 nm $\times$ 4.34nm $\times$ 17.38 nm

silicon was divided into several layers along the direction of laser. Then, the number of particles in each layer was counted, and the laser energy absorbed in each layer was allocated to each particle such that the kinetic energy of each particle is increased.

The dimensions of silicon bulk for the present simulations are $x = 8.69$ nm, $y = 4.34$ nm, $z = 8.69$ nm, and the parameters of the simulations in this paper are shown in Table 1. Pulse length (100 fs) was chosen for the studies of the simulation with a laser focus of 43.4 Å,[6] where the setup is necessary due to limitations in current computational power compared with experiments. Where applicable, the pulse energy was 0.02 J/cm^2 when taking the scaled absorption coefficient into account.

The time step was set to be 0.5 fs and set the initial atomic velocity to a Maxwell–Boltzmann distribution according to the temperature of the lattice which was initialized to $T_0 = 300$ K. The computational area had the same dimensions as the silicon bulk in directions x and y, but as twice as the silicon bulk in direction z. Any particle leaving the computational area was taken out of the simulation model to reduce the computational time that the maximum time-scale in the following simulations is 2.08 ps.

Particle interaction

As shown in Figure 3(a), silicon is assumed to have a crystal structure.[15] The Stillinger–Weber (SW) potential[16] is used because of its moderate cutoff radius, less parameters and simple form. In addition, the parameters of SW potential are taken from Holenstein et al.[17] to describe the interactions among the particles in this study. As shown in equation (2), the potential energy is given by

$$U = U_2(r_{ij}) + U_2(r_{ik}) + U_3(r_{ij}, r_{ik}, \theta_i) \tag{2}$$

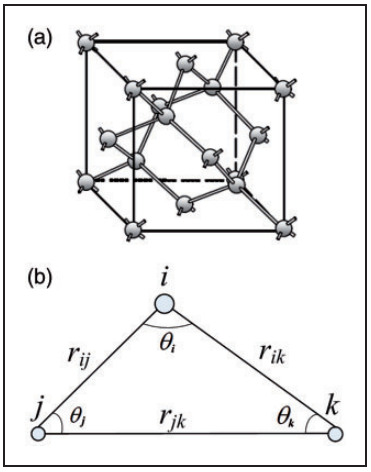

Figure 3. (a) Structure of Si(100) and (b) geometry of triplet of atoms used in definition of three-body potentials.

The SW potential has two-body and three-body interactions which are given by

$$\begin{cases} U_2(r_{ij}) = \left(A_1 r_{ij}^{-4} - A_2\right) \exp\left[\dfrac{\sigma}{r_{ij} - a}\right] \\ U_2(r_{ik}) = \left(A_1 r_{ik}^{-4} - A_2\right) \exp\left[\dfrac{\sigma}{r_{ik} - a}\right] \\ U_3(r_{ij}, r_{ik}, \theta_i) = \lambda \exp\left(\dfrac{\gamma\sigma}{r_{ij} - a}\right) \exp\left(\dfrac{\gamma\sigma}{r_{ik} - a}\right) \\ \qquad \cdot \left(\cos\theta_i + \dfrac{1}{3}\right)^2 \end{cases} \tag{3}$$

where $U_2(r_{ij})$ and $U_3(r_{ij}, r_{ik}, \theta_i)$ represent two-body and three-body interactions, respectively. r_{ij} is the distance between two atoms i and j; r_i, r_j and r_k represent the position vectors of atoms i, j and k, respectively. θ_i denotes the bonding angle defined in a similar manner as shown in Figure 3(b). The potential is cut abruptly to zero with a where $a = 0.377$ Å. $A_1 = 189.36$ eVÅ,[4] $A_2 = 16.32$ eV, $\lambda = 48.61$ eV, $\gamma = 1.2$ and $\sigma = 2.095$ Å are all constant.[17]

Adams velocity algorithm

The fourth-order Adams velocity algorithm[18] was used as the predictor formula and corrector formula as shown in equations (4) and (5), so that more particles can be studied within the same period of time to enable the implementation of MD simulation

$$\begin{cases} \vec{a}_i'(t) = \dfrac{1}{m_i} \vec{F}_i(\vec{r}(t)) \\ \vec{v}_i'(t + \Delta t) = \vec{v}_i(t) + \dfrac{\Delta t}{24}(55\vec{a}_i'(t) - 59\vec{a}_i(t - \Delta t) \\ \quad + 37\vec{a}_i(t - 2\Delta t) - 9\vec{a}_i(t - 3\Delta t)) \\ \vec{r}_i'(t + \Delta t) = \vec{r}_i(t) + \dfrac{\Delta t}{24}(55\vec{v}_i(t) - 59\vec{v}_i(t - \Delta t) \\ \quad + 37\vec{v}_i(t - 2\Delta t) - 9\vec{v}_i(t - 3\Delta t)) \end{cases} \tag{4}$$

$$\begin{cases} \vec{a}_i(t+\Delta t) = \dfrac{1}{m_i}\vec{F}_i\left(\vec{r}\,'(t+\Delta t)\right) \\ \vec{v}_i(t+\Delta t) = \vec{v}_i(t) + \dfrac{\Delta t}{24}(9\vec{a}_i(t+\Delta t) + 19\vec{a}_i(t) \\ \quad -5\vec{a}_i(t-\Delta t) + \vec{a}_i(t-2\Delta t)) \\ \vec{r}_i(t+\Delta t) = \vec{r}_i(t) + \dfrac{\Delta t}{24}(9\vec{v}_i(t+\Delta t) + 19\vec{v}_i(t) \\ \quad -5\vec{v}_i(t-\Delta t) + \vec{v}_i(t-2\Delta t)) \end{cases} \tag{5}$$

Boundary conditions

One of the problems with the simulation of real solid surfaces is the limited length of the MD simulation box and the flow of heat out of the lower boundary in latter time during the ablation. So, periodic boundary conditions were applied in x-direction and y-direction during the simulation.[17] However, if not properly handled, the lower boundary can lead to overheating or overcooling of the simulation region. The lower boundary connects to the continuum solid material and in order to properly calculate the heat flow (HF) into the underlying solid a HF calculation for the solid continuum is also carried out and coupled to the MD simulation at the lower boundary. The HF system in turn was connected to a heat bath set to 300 K, to simulate an infinite bulk medium.[17]

The MD and HF systems were energetically coupled as illustrated in Figure 4. A section at the bottom of the MD system (~2.6 nm) overlaps with the top of the HF system. The MD particles in the bottom region (~1.0 nm) are damped to the temperature obtained from the HF model. Under the above-mentioned boundary condition, the temperature of the particles at the bottom of the MD model is kept the same as the temperature in the region of HF model, which could be used to avoid either self-heating or self-cooling. Damping was fulfilled using Langevin dynamics.[19,20] The force on the atoms is given by

$$m_k\ddot{\vec{r}}_k = \vec{F}_k\left(\vec{r}_1,\ldots,\vec{r}_N,\right) - m_k\gamma_k\dot{\vec{r}}_k + \vec{R}_k \tag{6}$$

where $\vec{F}_k\left(\vec{r}_1,\ldots,\vec{r}_N\right)$ are the original forces derived from SW potential function, $\vec{R}_k = \sqrt{2\gamma_k k_B T m_k}\vec{\eta}_k$ denotes the random white noise forces in which $\vec{\eta}_k$ are vectors of Gaussian random numbers centered at zero. Negative term $(-m_k\gamma_k\dot{\vec{r}}_k)$ represents a damping term, and $\gamma_k = \pi k_B\theta_D$ and $\theta_D = 645$ K represent the Debye temperature of silicon. The positive term represents the gained energy due to the collision of particles in the thermal bath. In equilibrium, collisions occurred among the particles in these two regions such that the energy was exchanged between them. Consequently, these two regions reached the same temperature T which is obtained from the overlap part of the MD and HF coupled model as showed in Figure 4.

The coupling model was verified by Holenstein et al.[17] via keeping a constant surface temperature. Surface atoms were continually damped to 1200 K. In addition, the temperature evolution of the system was observed, and the continuous isotherms were obtained. Holenstein et al.[17] concluded that the coupling mode was performed adequately and was more accurate than any other boundary condition for this application.

As shown in Figure 4 and stated above, the overlapped area between MD and HF models was divided into two parts: The top portion of the bulk (in pink) shows the temperature profile of the MD system, and the bottom portion (in gray) represents the HF system, as indicated in the figure. The scales of top and bottom parts along the direction of laser irradiation were about 1.629 nm and 1.086 nm, respectively.

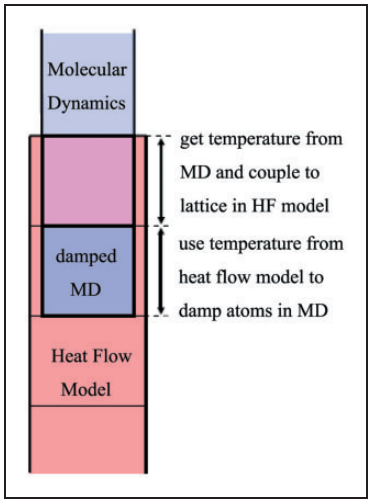

Figure 4. Molecular dynamics-heat flow hybrid model: Layout of interfacing. The interface (overlap) region is on the order of a few nanometers.
MD: molecular dynamics; HF: heat flow.

Physical statistics

Kinetic energy E_k, potential energy U, total energy E and temperature T were all investigated during the simulations. U was determined using SW potential, and E_k, E and T were computed by the following equations

$$\begin{cases} E_k = \dfrac{1}{2}\displaystyle\sum_{i=1}^{N} m_{i_i}^2 \\ E = E_k + U \\ T = \dfrac{1}{3N_B}\displaystyle\sum_{i=1}^{N} m_{i_i}^2 \end{cases} \tag{7}$$

where m_i, r_i and v_i represent the mass, position and velocity of atom i, respectively. N denotes the number of atoms, and k_B is the Boltzmann coefficient.

In addition, Cell-index Method and Neighbor List Method[18] were also used during the simulation to reduce the computational time. For this method, the whole bulk was divided into unit cells with the dimensions of 0.543 nm × 0.543 nm × 0.543 nm which were equal to the lattice constant of silicon.

As showed in Figure 5, the physical parameters of all the particles in the unit cells are represented by the center of the cell for the planer distribution used in our simulations. The sampling length was set to be the lattice constant for our latter simulations.

Results

When the light spot was less than the investigated surface in area, the silicon surface rose due to the thermal expansion induced by the laser absorption. Molten atoms flowed out from the molten pool and gathered around the hole. The silicon surface was investigated in details after the ablation water-jet cooling technique is employed to achieve this goal. It was observed that the phenomena of the propagation of the thermal wave which could lead to irregular deformation of silicon, such as dislocations and vacancies. The nonuniform distribution of laser could affect the processing quality of silicon.

Density variation

It can be seen from Figure 6(a) that the lattice has a regular array in silicon. As shown in Figure 6(b), the surface rose due to the thermal expansion induced by laser irradiation. Molten atoms flowed out from the molten pool and gathered around the hole. As a result, a convex hole was formed in the top surface of silicon.

Laser energy was deposited on each atom according to the Lambert–Beer's law, which enabled the surface atoms to acquire maximum energy. The less laser energy absorbed by an atom decreased as its distance from the surface increased.

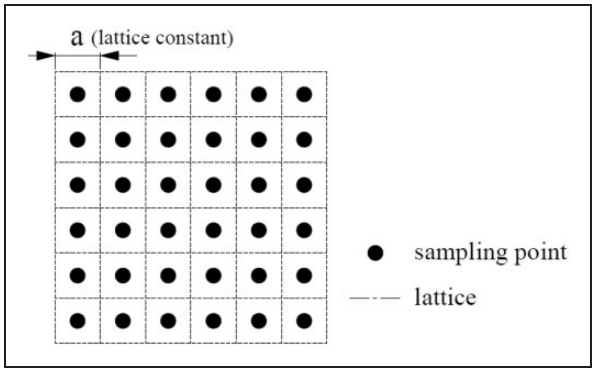

Figure 5. Sampling sketch for planer distribution of physical statistics.

Propagation of thermal wave

Thermal wave (range from 1000 K to 28,000 K) generated after laser irradiation, which we can seen from Figure 7. It gradually spread vertically downward since 1.35 ps from the beginning. Moreover, the propagation of thermal wave could lead to irregular deformation of silicon. Therefore, the effect of water-jet cooling on the ablation of silicon was investigated. In addition, in order to clearly observe the propagation of density distribution, we depicted the value of temperature along the vertical direction at the middle of x-coordinate which is illustrated in Figure 8. Furthermore, speed of thermal wave was calculated by the data depicted in Figure 9. The least squares fitting of the data line in the graph is $z_{Tpeak}(\text{nm}) = -6.483t(\text{ps}) + 9.2969$. Then, the speed of thermal wave which is approximate 6483 m/s which is close to the weighted average of the acoustic phonon velocities of 6533 m/s[20] in Si(100). It is attributed that the

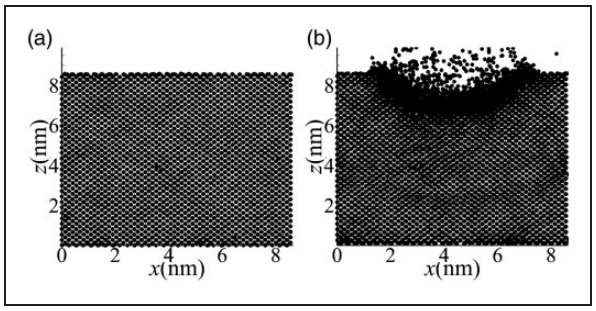

Figure 6. Shapes of silicon (a) before and (b) after ablation of silicon without water-jet cooling.

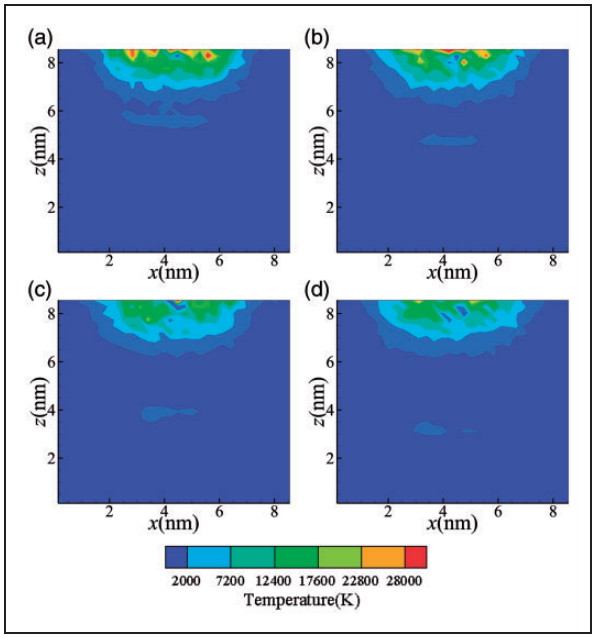

Figure 7. Two-dimensional distribution of thermal wave at different time without water-jet cooling. (a) Time 1.35ps (b) Time 1.45ps (c) Time 1.55ps and (d) Time 1.65ps

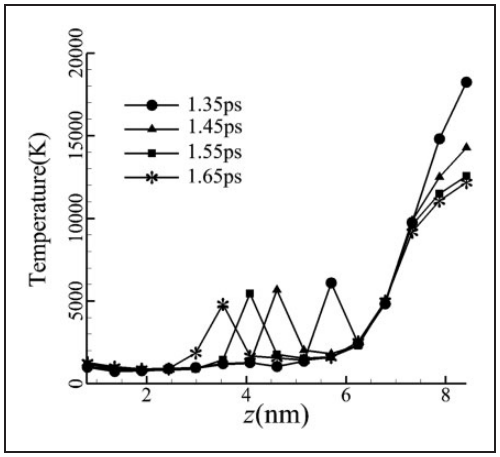

Figure 8. One-dimensional distribution (value of middle of the silicon buck along *x*-coordinate) of thermal wave versus time without water-jet cooling.

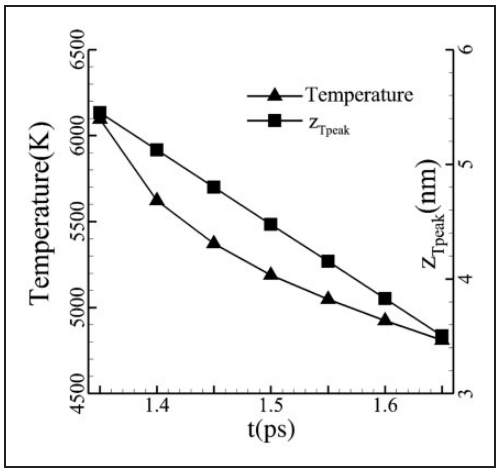

Figure 9. Propagation of thermal wave and variation of temperature amplitude (value of middle of the silicon buck along *x*-coordinate) versus time without water-jet cooling.

phonon energy transport thermal propagation direction dominates the other directions.

Propagation of density distribution

The density increased due to the melting of silicon under the effect of thermal wave. In addition, the peak density decreased as time increased. The number density of the surface gradually decreased as time increased. After laser irradiation, a density wave was generated and spread to the inner part of silicon. In addition, the number density of the surface gradually decreased, and the amplitude of the density wave reduced and disappeared eventually which was investigated from Figures 10 and 11. The distribution of density is clearly seen from these two figures which transmitted from surface of the silicon to the inner part. The amplitude of the density is almost remain the same versus the time. What is more, we can depict the position of the peak value of the density which is

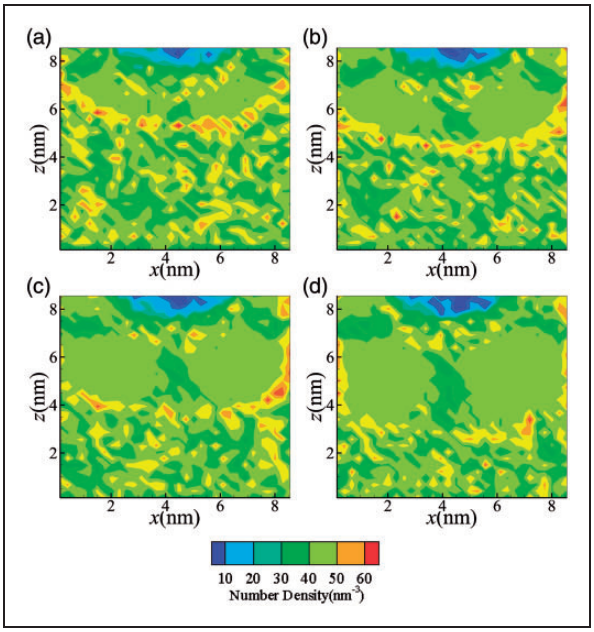

Figure 10. Two-dimensional distribution of density wave at different time without water-jet cooling (a) Time 1.35ps (b) Time 1.45ps (c) Time 1.55ps and (d) Time 1.65ps.

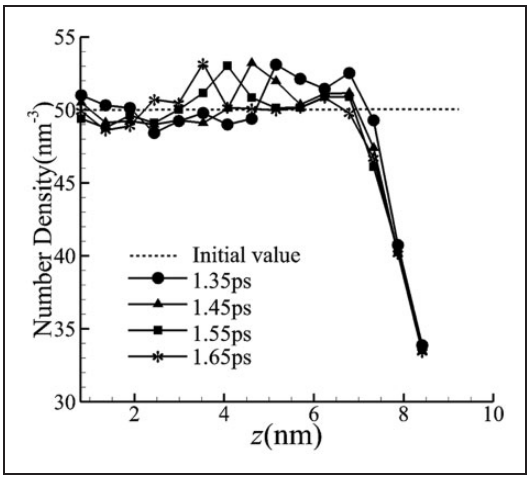

Figure 11. One-dimensional distribution of density wave (value of middle of the silicon buck along *x*-coordinate) at different time without water-jet cooling.

illustrated in Figure 12, The least squares fitting of the data line in the graph is $z_{Dpeak}(\text{nm}) = -6.932t(\text{ps}) + 14.8067$. Then, the speed of density wave which is approximately 6932 m/s, which is very closed to the propagation speed of thermal wave, confirms the melting of silicon by thermal wave.

Effect of water-jet cooling

Propagation of thermal wave. The propagation of thermal wave during laser irradiation would lead to the phase transformation which involved the melting and resolidification of silicon such that the original crystal structure of silicon could not be maintained. Then, in

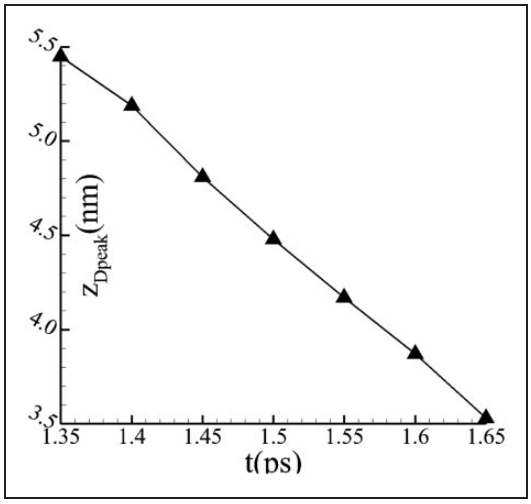

Figure 12. Propagation speed of density wave (value of middle of the silicon buck along *x*-coordinate) without water-jet cooling.

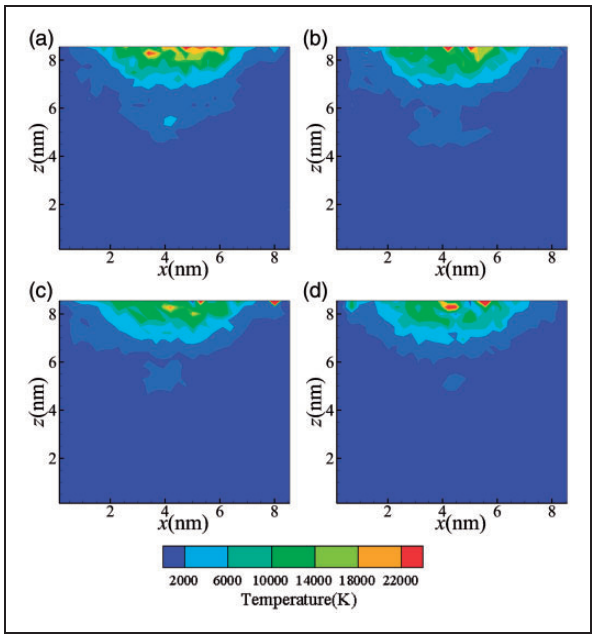

Figure 13. Two-dimensional distribution of thermal wave with water-jet cooling (a) Time 1.35ps (b) Time 1.45ps (c) Time 1.55ps and (d) Time 1.65ps.

order to decrease this thermal deformation, water-jet cooling technique was employed in the following simulations. The MD and HF models were also energetically coupled to simulate the effect of water-jet cooling at the boundary of the silicon bulk. As shown in Figure 1, water is jetted on both sides of silicon model to reduce the temperature of particles along boundary. We expect that the thermal-affected zone reduced and vanished faster than the case without water-jet cooling. Furthermore, the water-jet cooling diminished the heat in the ablated area of the surface such that the lower part could maintain its original structure to the greatest extent.

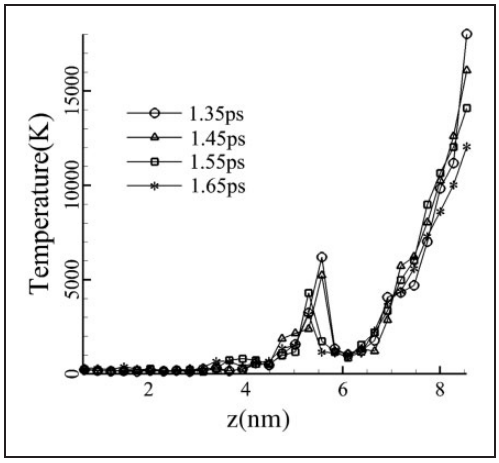

Figure 14. One-dimensional distribution of thermal wave at different time with water-jet cooling.

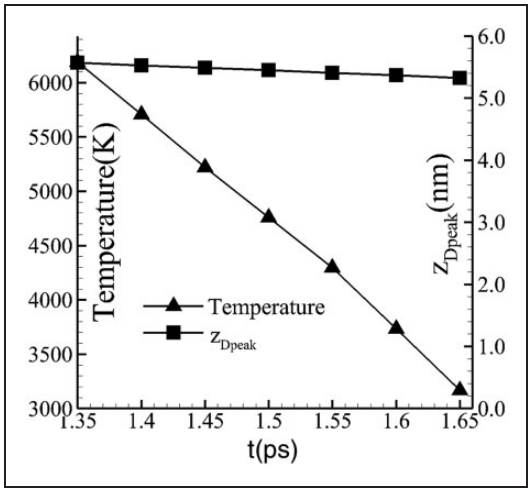

Figure 15. Propagation speed of thermal wave and variation of temperature amplitude at different time with water-jet cooling.

The area of the thermal wave gradually became smaller versus time in Figure 13. It is more convenient to see the variation while the temperature along the *z*-direction is extracted at the middle position of *x*-coordinate which is illustrated in Figure 14. Moreover, compared with the case without water-jet cooling in Figure 7, the location of thermal wave peak almost unchanged and the amplitude of the four different time are all smaller than those of the previous case. Four lines represented the temperature distribution of different time in this figure almost overlap together which accounts for the amplitude of temperature and position of the peak are almost constant. What is more, Figure 15 is depicted to calculate the propagation speed of the thermal wave in this case with the water-jet cooling. Obviously, the *z*-coordinate of the thermal wave is almost stay fixed. Thanks to the addition of cooling water, it has good inhibitory effect on the propagation of thermal wave on the ablation of silicon.

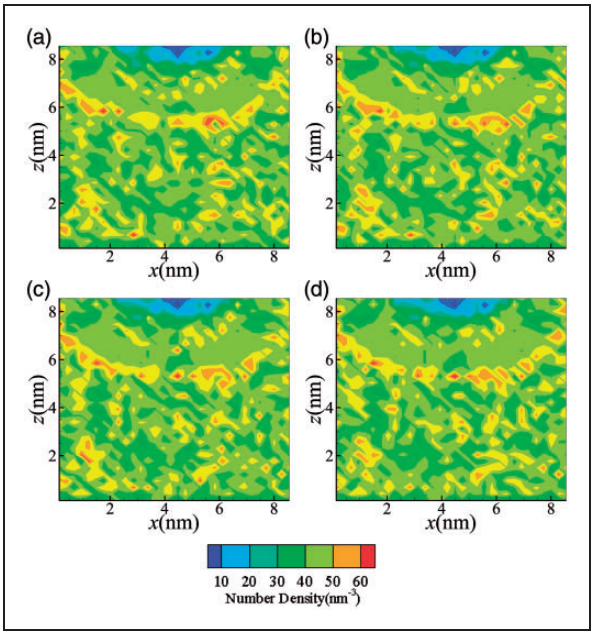

Figure 16. Two-dimensional distribution of density wave with effect of water-jet cooling (a) Time 1.35ps (b) Time 1.45ps (c) Time 1.55ps and (d) Time 1.65ps.

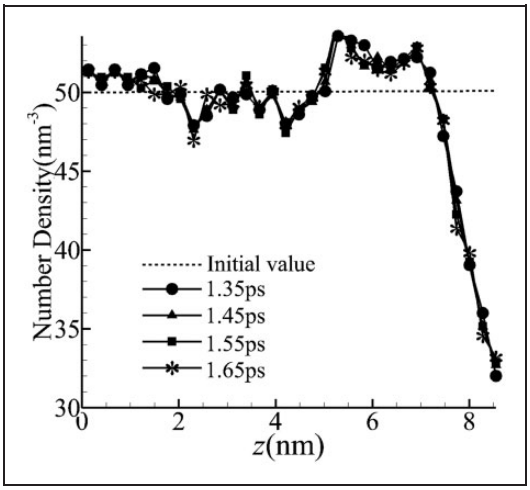

Figure 17. One-dimensional distribution of density wave with water-jet cooling.

Propagation of density distribution. Because of crystal structure change is ultimately reflected on the change of the position of particles. Then, we also study the change of density distribution over time accompanied with the water-jet cooling on the ablation of silicon. As shown in Figure 16, the variation of the density became slighter compared the case without water-jet cooling in Figure 10. The line on the figure almost overlapped together. Together with Figure 17 and Figure 18, the position of the peak value of density is confined to the area above about 5.2 nm at the z-coordinate. So, water-jet is quiet helpful to reduce the damage of thermal wave during ablation of silicon. And then, the silicon can, as far as possible, keep its original crystal structure.

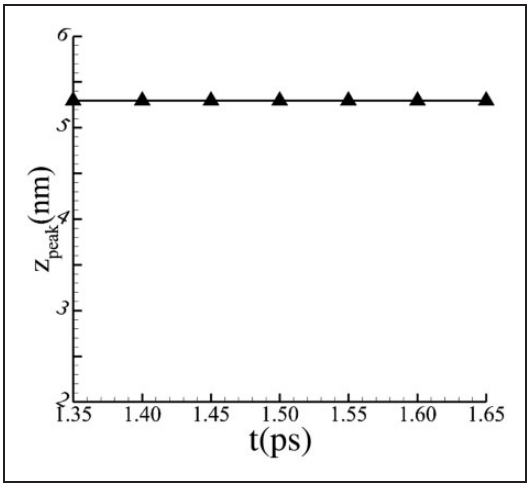

Figure 18. Propagation speed of density wave with water-jet cooling.

Conclusions

The ablation of silicon by fs-laser irradiation was simulated using a combined MD and one-dimensional HF model. Langevin dynamics was utilized to couple HF and MD models. It could be seen from the presentation above that:

1. The propagation speed of laser induced thermal wave was about 6483 m/s, which was close to the weighted average transverse acoustic phonon speed of 6533 m/s in Si(100), which meant that the transmission of phonon energy dominates the other transmission ways;
2. The propagation speed of density wave was about 6932 m/s which was almost the same as the speed of thermal wave on account of the melt of thermal effect. The two-dimensional thermal wave gradually spread vertically downward;
3. The propagation area of thermal wave was reduced and vanished faster with the effect of water-jet cooling than without water-jet cooling;
4. The water-jet cooling diminished the heat in the ablation area of the surface such that the lower part can maintain its original structure. It could therefore be concluded that the water-jet cooling technique could be used to considerably improve the ablation quality of silicon.

Declaration of conflicting interests

The author(s) declared no potential conflicts of interest with respect to the research, authorship, and/or publication of this article.

Funding

The author(s) disclosed receipt of the following financial support for the research, authorship, and/or publication of this article: The work described in this paper was fully

supported by a grant from Shenzhen Technology Project (Project No. JCYJ20140417172417123, JCYJ201 50529115038093).

References

1. Sugioka K and Cheng Y. Femtosecond laser processing for optofluidic fabrication. *Lab Chip* 2012; 12: 3576–3589.
2. Sibailly OD, Wagner FR, Mayor L, et al. High precision laser processing of sensitive materials by Microjet[C]// Fourth International Symposium on Laser Precision Microfabrication. *International Society for Optics and Photonics*, 21–24 June 2003, pp.501–504. Munich, Germany.
3. Ohmura E, Fukumoto I and Miyamoto I. Molecular dynamics simulation of ablation process with ultra-short-pulsed laser[C]//First International Symposium on Laser Precision Microfabrication (LPM2000). *International Society for Optics and Photonics*, 14 June 2000, pp.84–89. Omiya, Saitama, Japan.
4. Richerzhagen B. Industrial applications of the water-jet guided laser. *Ind Laser User* 2002; 28: 28–30.
5. Le Barillec O, Davenet M, Favre A, et al. Advanced vacuum wafer drying for thermal laser separation dicing assessment results from European collaborative seal project. *Solid State Phenomena* 2013; 195: 252–257.
6. Herrmann R, Gerlach J and Campbell E. Ultrashort pulse laser ablation of silicon: an MD simulation study. *Appl Phys A* 1998; 66: 35–42.
7. Ho J, Grigoropoulos C and Humphrey J. Computational study of heat transfer and gas dynamics in the pulsed laser evaporation of metals. *J Appl Phys* 1995; 78: 4696–4709.
8. Watanabe K, Ishizaka Y, Ohmura E, et al. Analysis of laser ablation process in semiconductor due to ultra-short-pulsed laser with molecular dynamics simulation[C]//Symposium on High-Power Lasers and Applications. *International Society for Optics and Photonics*, 2000, pp.46–55.
9. Ivanov DS and Zhigilei LV. Combined atomistic-continuum modeling of short-pulse laser melting and disintegration of metal films. *Phys Rev B* 2003; 68: 064114.
10. Zhigilei LV, Leveugle E, Garrison BJ, et al. Computer simulations of laser ablation of molecular substrates. *Chem Rev* 2003; 103: 321–348.
11. Jeschke HO, Garcia ME, Lenzner M, et al. Laser ablation thresholds of silicon for different pulse durations: theory and experiment. *Appl Surf Sci* 2002; 197: 839–844.
12. Lorazo P, Lewis LJ and Meunier M. Short-pulse laser ablation of solids: from phase explosion to fragmentation. *Phys Rev Lett* 2003; 91: 225502(1)–225502(4).
13. Li C, Johnson D and Kovacevic R. Modeling of water-jet guided laser grooving of silicon. *Int J Mach Tools Manufact* 2003; 43: 925–936.
14. Pfeiffer HG and Liebhafsky HA. The origins of beer's law. *J Chem Educ* 1951; 28: 123–125.
15. Balamane H, Halicioglu T and Tiller W. Comparative study of silicon empirical interatomic potentials. *Phys Rev B* 1992; 46: 2250–2279.
16. Stillinger FH and Weber TA. Computer simulation of local order in condensed phases of silicon. *Phys Rev B* 1985; 31: 5262–5271.
17. Holenstein R, Kirkwood SE, Fedosejevs R, et al. Simulation of femtosecond laser ablation of silicon. *Proc SPIE* 2004; 5579: 688–695. DOI: 10.1117/12.567675.
18. Beeman D. Some multistep methods for use in molecular dynamics calculations. *J Comput Phys* 1976; 20: 130–139.
19. Adelman S and Doll J. Generalized Langevin equation approach for atom/solid-surface scattering: general formulation for classical scattering off harmonic solids. *J Chem Phys* 1976; 64: 2375–2388.
20. Haberland H, Insepov Z and Moseler M. Molecular-dynamics simulation of thin-film growth by energetic cluster impact. *Phys Rev B* 1995; 51: 11061–11067.